Journal of Molecular Structure 1348 (2025) 143476

Contents lists available at ScienceDirect

Journal of Molecular Structure

journal homepage: www.elsevier.com/locate/molstr

Rational design of donor–acceptor (D-A) conjugated microporous polymers containing thienopyrene and triazine building units for enhanced photocatalytic hydrogen production

Shymaa Mostafa Ebrahium [a], Yang-Chin Kao [b], Haitham M El-Bery [a], Osama Younis [c], Ahmed A.K. Mohammed [a], Kamal I. Aly [a,*], Shiao-Wei Kuo [b,d,**], Mohamed Gamal Mohamed [a,b,**]

[a] Department of Chemistry, Faculty of Science, Assiut University, Assiut 71516, Egypt
[b] Department of Materials and Optoelectronic Science, Center for Functional Polymers and Supramolecular Materials, National Sun Yat-Sen University, Kaohsiung 804, Taiwan
[c] Chemistry Department, Faculty of Science, the New Valley University, El-Kharja, 72511, Egypt
[d] Department of Medicinal and Applied Chemistry, Kaohsiung Medical University, Kaohsiung 807, Taiwan

ARTICLE INFO

Keywords:
Pyrene
Thiophene
Triazine
Conjugated Microporous Polymers
Photocatalysis
Hydrogen Evolution
Water Splitting

ABSTRACT

Conjugated microporous polymers (CMPs) represent a rapidly advancing group of metal-free organic photocatalysts, offering a sustainable route for hydrogen (H_2) generation through photocatalytic water splitting. Their intrinsic permanent porosity, combined with extended π-conjugation and large surface areas, enables superior light harvesting, efficient exciton dissociation, and accelerated molecular diffusion—key attributes for effective photocatalytic systems. In this study, two newly developed CMPs—Py–Thio–Tri CMP and Py–Thio–PyD CMP—were synthesized and subjected to rigorous physicochemical characterization to investigate their photocatalytic performance. Nitrogen adsorption–desorption measurements were employed to determine their porosity. The chemical structures and functional group integrity were validated via Fourier-transform infrared (FT-IR) spectroscopy. Photocatalytic evaluations demonstrate that Py–Thio–Tri CMP exhibits markedly superior hydrogen evolution activity compared to Py–Thio–PyD CMP. Specifically, Py–Thio–Tri CMP achieves an initial hydrogen generation rate (HGR) of 1100 μmol h^{-1} g^{-1} within the first hour of irradiation, substantially surpassing the 182 μmol h^{-1} g^{-1} recorded for Py–Thio–PyD CMP under similar circumstances. Upon incorporation of 3 wt % cobalt (Co) as a cocatalyst, the HGRs further increased to 1242 and 249 μmol h^{-1} g^{-1} for Py–Thio–Tri CMP and Py–Thio–PyD CMP, respectively. Additionally, transient photocurrent response and electrochemical impedance spectroscopy (EIS) measurements corroborate Py–Thio–Tri CMP enhanced photogenerated carrier mobility and suppressed charge recombination dynamics.

1. Introduction

Hydrogen (H_2) plays a pivotal role in the global shift toward clean energy, offering a viable alternative to fossil fuels across various industrial and energy sectors [1–6]. With its high energy density and zero-emission combustion, hydrogen is considered a key solution for reducing greenhouse gas emissions and addressing climate change [7–11]. Despite advancements, traditional techniques like coal gasification(CG) and steam methane reforming (SMR) remain common for H_2 generation, generating significant CO_2 emissions, raising concerns about their sustainability [12–15]. As a result, researchers are increasingly focusing on green hydrogen production methods that utilize renewable resources and advanced catalytic materials to enhance efficiency while minimizing environmental impact [12–15]. Among the emerging hydrogen production technologies, photocatalytic and electrocatalytic water splitting have gained significant interest due to their

* Corresponding author.
** Corresponding authors: Department of Materials and Optoelectronic Science, Center for Functional Polymers and Supramolecular Materials, National Sun Yat-Sen University, Kaohsiung 804, Taiwan.
E-mail addresses: Kamalaly@aun.edu.eg (K.I. Aly), kuosw@faculty.nsysu.edu.tw (S.-W. Kuo), mgamal.eldin12@yahoo.com, mgamal.eldin12@aun.edu.eg (M.G. Mohamed).

https://doi.org/10.1016/j.molstruc.2025.143476
Received 20 June 2025; Received in revised form 23 July 2025; Accepted 26 July 2025
Available online 28 July 2025

ability to harness renewable energy sources, such as solar and wind power, for H_2 generation [16,17]. Photocatalytic water splitting offers a straightforward approach to H_2 production [18–20]. Effective polymeric photocatalysts require water stability, suitable energy levels, visible light absorption, efficient charge transport, and active catalytic surfaces [21–24].

The heavy dependence on fossil fuels has led to major energy crises and environmental problems, driving the search for cleaner, alternative energy solutions [25–28]. Water splitting is a clean and efficient method for H_2 production, emitting only oxygen as a byproduct. Photocatalytic water splitting stands out for its renewable and eco-friendly nature [29–32]. Various inorganic semiconductors, including metal oxides, nitrides, sulfides, and selenides, have been investigated for their strong photocatalytic performance and suitable electronic properties [33–35].

In recent years, CMPs have been seen as strong contenders for photocatalysts due to their robust and adaptable π-conjugated systems and permanent microporosity [36–40]. Their extended π-systems promote effective light absorption and charge transport, while the porous framework offers high surface area and accessible catalytic sites [41–48]. These features make CMPs excellent candidates for visible-light-driven HER [49]. Among the various building blocks used in CMP design, pyrene and triazine units have emerged as particularly effective components for photocatalytic H_2 production. Py is a polycyclic aromatic hydrocarbon known for its strong π-conjugation, high electron mobility, and broad absorption in the visible spectrum, which are beneficial for light harvesting and charge transport in photocatalytic systems [50–52]. Triazine, a nitrogen-rich heterocyclic unit, contributes electron-deficient characteristics, enhancing charge separation and improving the interaction with water molecules during catalysis [53]. The combination of pyrene and triazine units within CMPs allows for the construction of donor–acceptor-type frameworks that promote efficient charge carrier separation and prolong charge lifetimes—critical factors for enhanced HER activity [51]. The research team led by Mohamed et al. has been at the forefront of developing CMPs tailored for H_2 evolution. In a notable study, they synthesized Py–TPA-CMP via Sonogashira–Hagihara coupling, with Py–TPA-CMP showing the highest HER of 19200 μmol h^{-1} g^{-1} and an apparent quantum yield of 15.3 % under visible light [50]. Building on this work, the research group designed donor–π–acceptor CMPs using an alkyne bridge as a strategy to suppress charge recombination. The resulting Py–TB–TPA CMP exhibited a HER of 16700 μmol h^{-1} g^{-1}, which was significantly improved due to better charge transport and longer-lived excitons [49]. In addition to pyrene-based systems, other architectures developed by Mohamed et al. and his team have demonstrated similar promise. For instance, CMPs incorporating thienyltriazine units have shown excellent HER performance and stability under prolonged light exposure [51]. These results suggest that rational design of CMPs, especially by tuning donor–acceptor interactions and bridge structures, is a key approach to boosting photocatalytic activity. Xie et al. synthesized a triazine CMP (CMP-1) showing a HER of 9698.13 μmol h^{-1} g^{-1} with excellent stability, attributing the performance to its optimized band structure and porosity [54].

In this work, we developed two photoactive CMPs [Py–Thio–Tri CMP and Py–Thio–PyD CMP] incorporating thienopyrene as an electron donor unit and triazine unit as a deficient electron, as depicted in Fig. 1. These CMPs were specifically designed to facilitate H_2 production through the photocatalytic splitting of water (H_2O). To comprehensively analyze their structural, morphological, and photophysical properties, we utilized FTIR spectroscopy, BET surface area analysis, photoluminescence (PL) spectroscopy, and TEM. These techniques enabled us to investigate the chemical composition, porosity, optical behavior, and thermal stability of the synthesized CMPs. The photocatalytic hydrogen evolution capabilities of the CMPs were subsequently tested under visible-light irradiation in the presence of ascorbic acid (AA) as a sacrificial agent (SA).

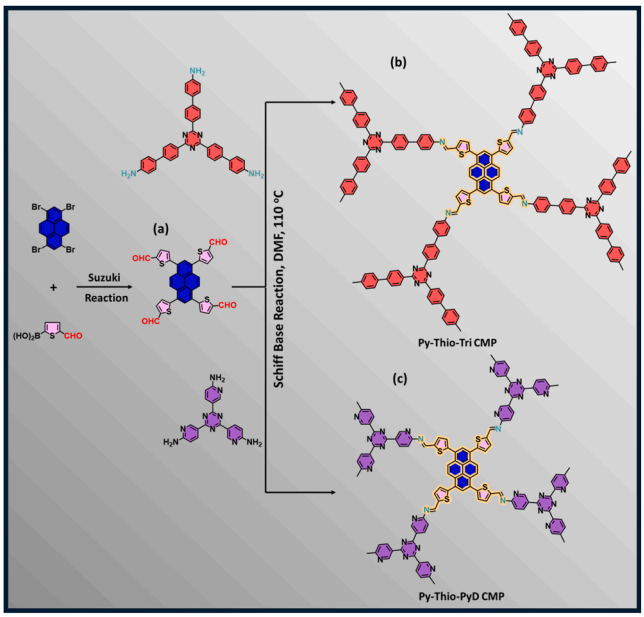

Fig. 1. synthesis of (a) Py-Thio-4CHO, (b) Py–Thio–Tri CMP and (c) Py–-Thio–PyD CMP.

2. Experimental section

2.1. Materials

Pyrene (Py), 6-Aminonicotinonitrile (6-Amino-NicCN), 4′-Aminobiphenyl-4-carbonitrile (4-Amino-BiCN), bromine (Br_2), nitrobenzene, trifluoromethanesulfonic acid [TFMSA], 5-formyl-2-thienylboronic acid [5-ThBO-CHO], potassium carbonate (K_2CO_3), 1,4-dioxane (anhydrous), palladium tetrakis(triphenylphosphine) [$Pd(PPh_3)_4$], methanol (MeOH), ethanol (EtOH), tetrahydrofuran (THF), acetone, N,N-dimethylformamide (DMF), hydrochloric acid (HCl), and other reagents were purchased from commercial suppliers (e.g., Sigma-Aldrich).

2.2. Synthesis of 1,3,6,8-Tetrabromopyrene (Py–Br_4) [49,55–57]

Py (3 g, 17.5 mmol) was reacted with Br_2 (4 mL) in nitrobenzene (60 mL) under reflux at 120 °C for 4 h, yielding a green precipitate (4.4 g, 89 %). FTIR (KBr, cm^{-1}): 3053 (sp^2 aromatic C–H).

2.3. Synthesis of 5,5′-(3,8-bis(4-formylcyclopenta-1,3-dien-1-yl)pyrene-1,6-diyl)bis(thiophene-2-carbaldehyde) [Py-Thio-4CHO] [58]

A mixture of Py-Br_4 (1.88 g, 3.83 mmol), $Pd(PPh_3)_4$ (0.21 g, 0.17 mmol), K_2CO_3 (8 g, 58 mmol), and 5-ThBO-CHO (3.41 g, 41.26 mmol) was degassed under vacuum. After the addition of 1,4-dioxane (80 mL) and deionized water (20 mL) in a 4:1 volume ratio, the reaction mixture was stirred at 85 °C for 48 h under a nitrogen atmosphere to ensure an inert environment. Upon completion, the reaction mixture was poured into 400 mL of ice-cold water to precipitate the product. The excess K_2CO_3 present in the mixture was neutralized by the gradual addition of 60 mL of HCl (2 M) with stirring. The resulting yellow precipitate was collected by vacuum filtration, washed thoroughly with water and methanol, and then dried under vacuum to yield the final solid product. [Fig. 1(a)]. FTIR (KBr, cm^{-1}): 3045 (C-H aromatic), 2815, 2725 (CHO), 1691 (C=O).

2.4. Synthesis of 4,4′,4′′-(1,3,5-triazine-2,4,6-triyl)tris(([1,1′-biphenyl]-4-amine)) [Tri-3NH_2]

4-Amino-BiCN (2.88 g, 23.33 mmol) was reacted with TFMSA (7.53

mL, 85.35 mmol) in 100 mL of $CHCl_3$ under nitrogen at –20 °C for 24 h, using a methanol/liquid nitrogen-cooled Dewar flask. After the reaction, the yellow oil formed was diluted with 250 mL of cold water, and the pH was adjusted to 8–12 using 0.2 M NaOH, leading to the precipitation of a yellow solid [2.4 g, Yield: 80 %, **Scheme S1**].

2.5. Synthesis of 5,5′,5′′-(1,3,5-triazine-2,4,6-triyl)tris(pyridin-2-amine) [PyD-3NH$_2$]

6-Amino-NicCN (2.51 g, 21.06 mmol) was treated with TFMSA (6.5 mL, 73.72 mmol) in 100 mL of $CHCl_3$ under nitrogen at –20 °C for 24 h using a methanol/liquid nitrogen-cooled Dewar flask. After the reaction, the mixture was diluted with 250 mL of cold water, and the pH was adjusted to 8–12 using 0.2 M NaOH, resulting in the precipitation of a dark gray solid. The solid was filtered, washed with ethanol, and recrystallized from THF to afford 1.96 g of a pale pink solid (Yield: 74 %, **Scheme S2**).

2.6. Synthesis of Py–Thio–Tri CMP and Py–Thio–PyD CMP

DMF (40 mL), Py-Thio-4CHO (0.3 g, 1 mmol), and Tri-3NH₂ (0.36 g, 1.33 mmol) or PyD-3NH$_2$ (0.22 g, 1.33 mmol) were reacted at 120 °C for 72 h to afford Py–Thio–Tri CMP [brown solid, Fig. 1(b)] and For, Py–-Thio–PyD CMP [an orange solid [Fig. 1(c)].

2.7. Characterization of Py–Thio–Tri CMP and Py–Thio–PyD CMP

The architecture of the obtained chemical products, Tri-3NH$_2$, PyD-3NH$_2$, and Py-Thio-4CHO, was confirmed through FTIR analysis, as shown in [Fig. 2(a) **and Figures S1 and S2**]. The FTIR spectrum of Tri-3NH$_2$ displayed characteristic peaks corresponding to the primary NH$_2$ group and sp^2 C-H bonds. These were recorded at 3422 and 3469 cm^{-1} (symmetric and asymmetric stretching), respectively, while sp^2 C-H stretching was observed at 3023 cm^{-1} [**Figure S1**]. Tri-3NH$_2$ (**Figure S2**) showed the proton signals at 8.70, 7.82, 7.54, 6.70, and 5.47 ppm, which are also attributed to aromatic protons and NH units.

For PyD-3NH$_2$, characteristic peaks corresponding to the primary NH$_2$ group and sp^2 C-H bonds were detected at 3359 and 3442 cm^{-1} (symmetric and asymmetric stretching), distinctively, with sp^2 C-H stretching observed at 3131 cm^{-1}[**Figure S3**]. PyD-3NH$_2$ exhibits distinct aromatic C-**H** and amino proton signals at 9.19 ppm, 8.49-8.50 ppm, 6.56-6.58 ppm, and 6.79 ppm, based on ^{1}H NMR data [**Figure S4**]. Similarly, the spectrum of Py-Thio-4CHO revealed a peak associated with the aldehyde group at 2853 cm^{-1} and sp^2 C-H stretching at 3076 cm^{-1} [Fig. 2(a)]. The ^{1}H NMR spectrum of Py-Thio-4CHO (**Figure S5**) shows a distinct signal at 10.05 ppm corresponding to the aldehyde protons (4H, CHO). The aromatic and thiophene protons appear as multiple peaks at 8.62, 8.55, 8.45, a multiplet between 8.37–8.29, followed by signals at 8.25, 7.83–7.77, and 7.75 ppm. In the ^{13}C NMR

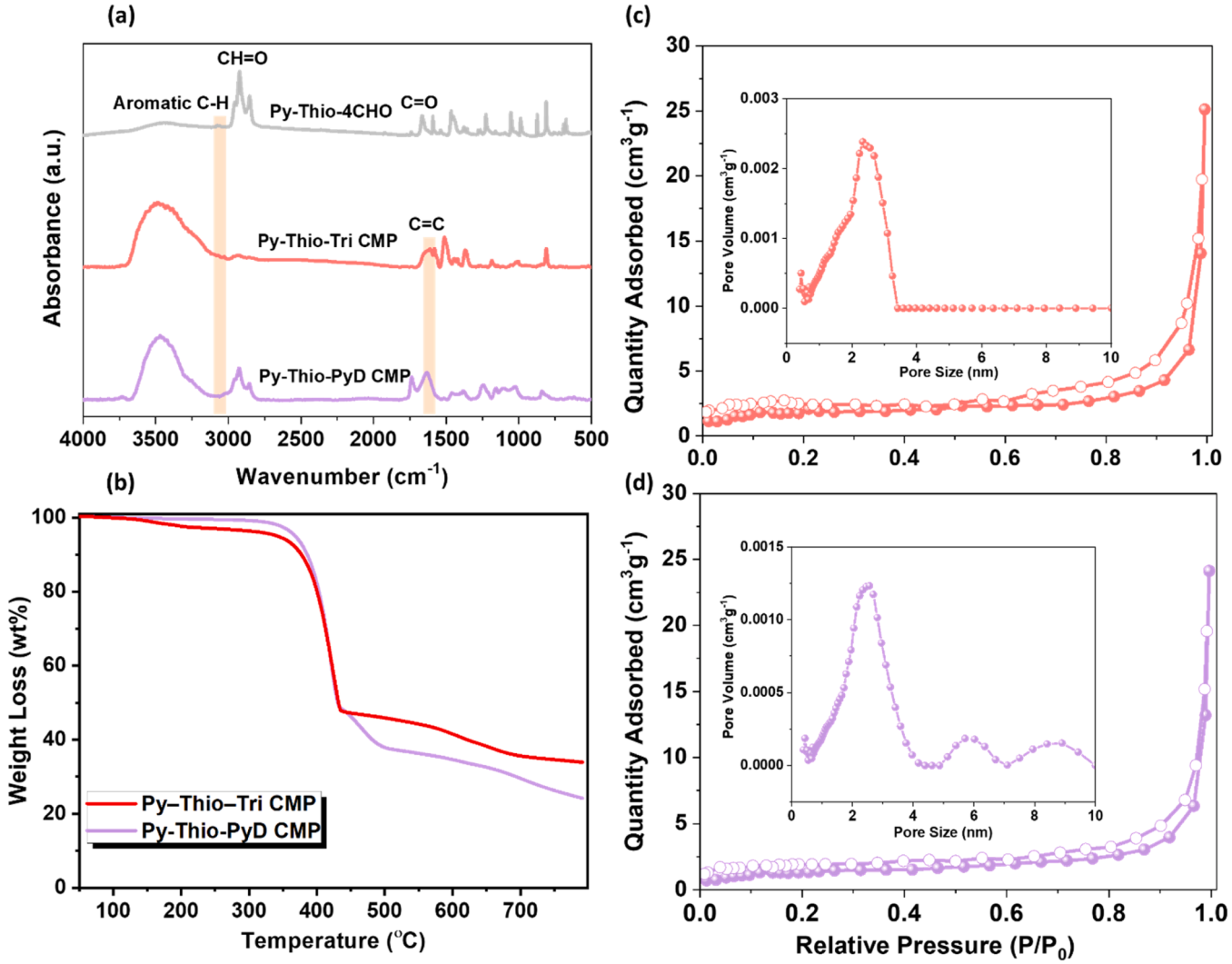

Fig. 2. (a) FTIR spectra of Py-Thio-4CHO, Py–Thio–Tri CMP and Py–Thio–PyD CMP. (b) TGA traces and (c, d) BET profiles of (b, c) Py–Thio–Tri CMP and (b, d) Py–Thio–PyD CMP.

spectrum (**Figure S6**), the aldehyde carbon is observed at 184.8 ppm, while the aromatic carbon signals are spread over the range of 143.8 to 119.15 ppm. Following the Schiff base reaction to synthesize and Py–-Thio–Tri and Py–Thio–PyD CMPs, their structures were verified through FTIR and TGA analysis. The FTIR spectrum of Py–Thio–PyD CMP presents a characteristic C=N bond at 1635 cm^{-1} and sp^2 C-H stretching at 3135 cm^{-1}.

Similarly, the spectrum of Py–Thio–PyD CMP unveiled C=N bonds at 1645 cm^{-1} and sp^2 C-H stretching at 3072 cm^{-1}. As shown in Fig. 2(b), TGA analysis revealed the T_{d10} values of Py–Thio–PyD CMP and Py–-Thio–Tri CMP to be 385 °C and 377 °C, with corresponding char yields of 24 wt. % and 34 wt. %, distinctively. The thermogravimetric analysis (TGA) results provide insights into the thermal stability and decomposition behavior of Py–Thio–Tri CMP and Py–Thio–PyD CMP. The differences in their thermal properties can be attributed to variations in their molecular structures, particularly the presence of biphenyl and pyridine units. The TGA curves indicate that Py–Thio–Tri CMP exhibits higher thermal stability than Py–Thio–PyD CMP. This enhanced stability can be attributed to the presence of triazine biphenyl in Py–Thio–Tri CMP, which contributes to a more extended π-conjugated network, enhancing the polymer's structural integrity and resistance to thermal decomposition. Nitrogen physisorption analysis was conducted to evaluate the surface area and porosity of Py–Thio–Tri CMP and Py–-Thio–PyD CMP. As illustrated in Fig. 2(c) and 2(d), both materials displayed Type III isotherm curves. The S_{BET} and total pore volume of Py–Thio–PyD CMP were measured to be 27 $m^2\ g^{-1}$ and 0.071 $cm^3\ g^{-1}$, respectively. The pore size distribution, determined using NLDFT, falls within the micro-mesoporous range (0.54-3.41 nm). In comparison, Py–Thio–Tri CMP exhibited an S_{BET} of 25 $m^2\ g^{-1}$ and a total pore volume of 0.174 $cm^3\ g^{-1}$, with the highest pore size distribution observed in the micro-mesoporous range (0.66-4.39 nm). High-resolution TEM images of Py–Thio–Tri CMP [Fig. 3(a–c)] reveal an irregular and amorphous morphology, indicative of its disordered network structure. Corresponding SEM-EDS elemental mapping [Fig. 3(d–f)] of carbon, nitrogen, and oxygen throughout the material. Similarly, TEM analysis of Py–-Thio–PyD CMP [Fig. 4(a–c)] displays a comparable disordered morphology. The accompanying SEM-EDS maps [Fig. 4(d–f)] further validate the even dispersion of C, N, and O elements within the framework.

2.8. Photophysical Behavior of Py–Thio–Tri CMP and Py–Thio–PyD CMP

The UV-visible absorption spectra of Py–Thio–Tri CMP and Py–-Thio–PyD CMP were measured in a solid state, as both polymers were insoluble in common organic solvents [Fig. 5]. The molecular structures of Py–Thio–Tri CMP and Py–Thio–PyD CMP exhibit extensive conjugation due to their aromatic and heterocyclic components, which significantly influence their optical properties. The UV-visible absorption spectra of the two polymers are remarkably similar, suggesting that the substitution of biphenyl units in Py–Thio–Tri CMP with pyridine rings in Py–Thio–PyD CMP does not significantly affect the primary electronic transitions. Both polymers display a main absorption band at 305 nm, which arises from π-π* transitions within their conjugated frameworks, dominated by the pyrene, thiophene, and triazine units. In addition to this primary band, two shoulder peaks are observed at 385 and 510 nm. These shoulders likely correspond to charge transfer (CT) transitions or n-π* transitions, reflecting the influence of donor-acceptor interactions within the CMP structures. Notably, both Py–Thio–Tri CMP and Py–-Thio–PyD CMP are almost transparent at wavelengths between 600 and 1100 nm, indicating the absence of low-energy electronic transitions in this range. This transparency highlights their potential for applications requiring materials with limited absorption in the near-infrared region. The absorbance values at 305 nm for Py–Thio–Tri CMP and Py–-Thio–PyD CMP indicate higher absorbance observed for Py–Thio–PyD CMP, which can be attributed to the electron-withdrawing nature of the pyridine rings compared to the biphenyl units in Py–Thio–Tri CMP. The replacement of biphenyl with pyridine enhances the overall conjugation and oscillator strength of Py–Thio–PyD CMP, thereby increasing its light absorption efficiency at this wavelength.

Tauc plot analysis [**Figure S7**] revealed optical band gaps of 1.93 eV for Py–Thio–Tri CMP and 1.9 eV for Py–Thio–PyD CMP, placing both within the optimal range for visible-light photocatalytic water splitting [59–61]. These results highlight the potential of donor–acceptor design to fine-tune light absorption and bandgap properties, while the electronic structure of the CMPs also plays a key role in enhancing photocatalytic H_2 production. The photoluminescence spectra of Py–Thio–Tri CMP and Py–Thio–PyD CMP were measured in a solid state at excitation wavelengths ranging from 330 to 360 nm to investigate their emission behavior and understand the role of structural variations on their optical properties [Fig. 6(a) and 6(b)]. Both CMPs exhibited similar

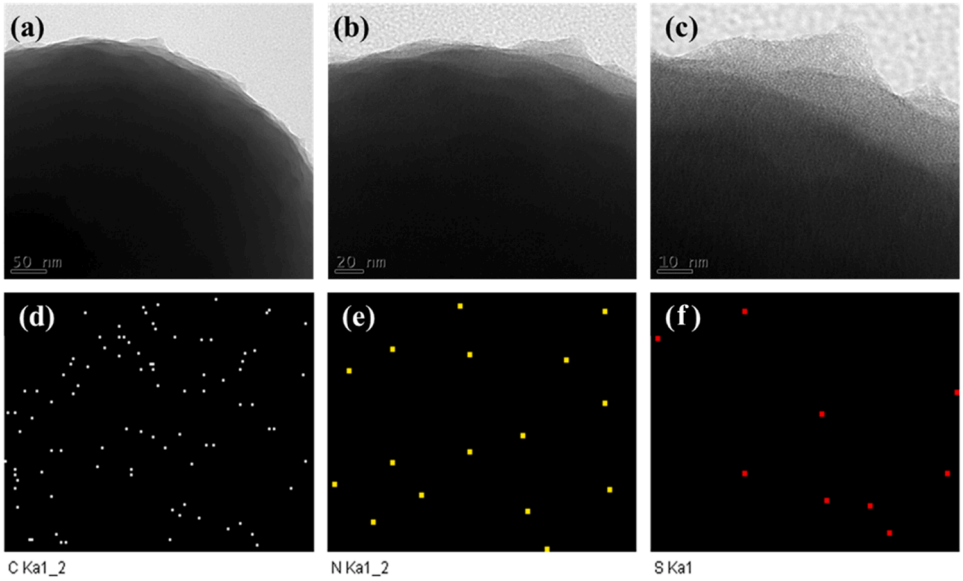

Fig. 3. (a–c) TEM images of the Py–Thio–Tri CMP framework, and (d-f) SEM–EDS elemental mapping images showing the distributions of (d) carbon (C), (e) nitrogen (N), and (f) sulfur (S) within the Py–Thio–Tri CMP framework.

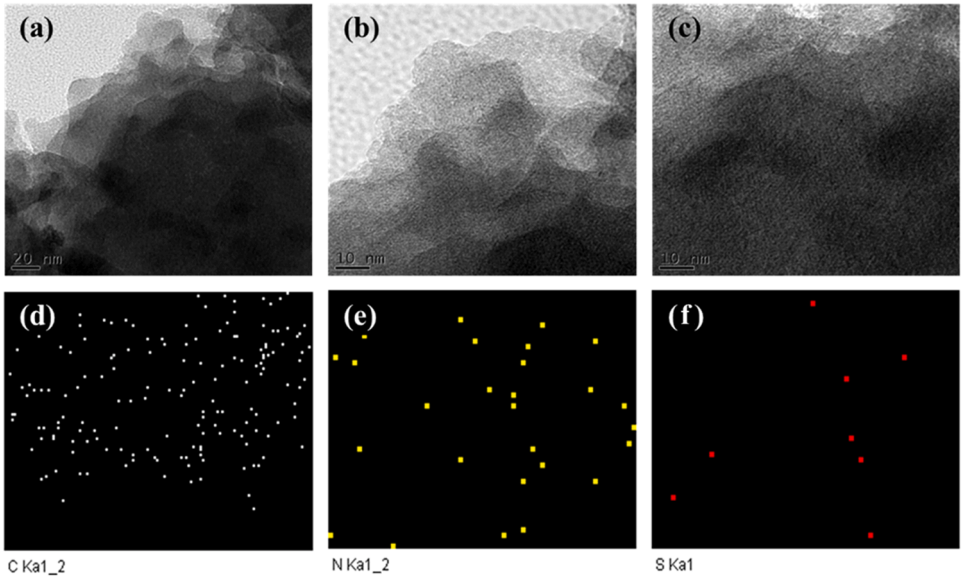

Fig. 4. (a-c) TEM images of the Py–Thio–PyD CMP framework, and (d-f) SEM–EDS elemental mapping images showing the distributions of (d) C, (e) N, and (f) S within the Py–Thio–PyD CMP.

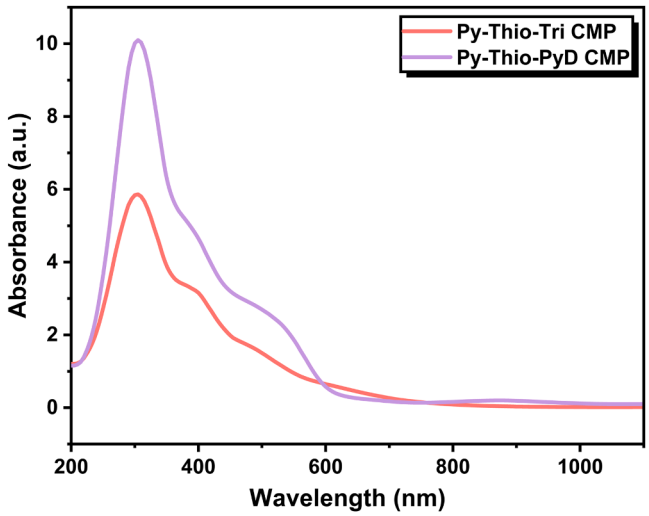

Fig. 5. UV-visible absorption spectra of the Py–Thio–Tri CMP and Py–-Thio–PyD CMP in the solid state.

photoluminescence behavior with a maximum emission between 490 and 495 nm, attributed to radiative decay from their lowest excited states. This consistency in the emission maxima suggests that the primary electronic transitions responsible for the emission are mainly unaffected by the substitution of biphenyl units in Py–Thio–Tri CMP with pyridine units in Py–Thio–PyD CMP. The observed emission in the blue-green region is likely due to the extended conjugation and strong donor-acceptor interactions within the polymer backbones. A notable distinction between the emission spectra of the two polymers was observed at wavelengths beyond 490 nm, where the excitation wavelength had a pronounced impact on the spectral profile. When the Py–Thio–Tri CMP and Py–Thio–PyD CMP were excited at 360 nm, the emission spectra showed a gradual decrease in intensity at wavelengths longer than 490 nm, indicating limited emission contributions from lower-energy states or vibrational relaxations. Conversely, excitation at 330 nm resulted in stronger emission intensities at longer wavelengths, producing a broader emission spectrum. This behavior suggests that excitation at higher-energy wavelengths (e.g., 330 nm) populates higher electronic states or engages secondary radiative pathways, potentially due to enhanced energy transfer within the polymer matrix or greater vibrational relaxation. In other words, this discrepancy suggests that the excitation energy at 360 nm may favor non-radiative relaxation pathways, leading to diminished emission in the longer wavelength range. In contrast, the excitation at 330 nm appears to promote more efficient radiative transitions, enhancing the overall emission intensity. The chromaticity coordinates derived from the CIE diagram further support these findings, offering a quantitative evaluation of the emission color for both Py–Thio–Tri CMP and Py–Thio–PyD CMP [Fig. 6(c)]. For Py–-Thio–Tri CMP, the coordinates at excitation wavelengths of 330 nm and 360 nm were (0.14, 0.49) and (0.10, 0.26), respectively. These results indicate a shift from a more greenish-blue emission at lower excitation energy (360 nm) to a purer blue emission at higher excitation energy (330 nm). Similarly, Py–Thio–PyD CMP exhibited chromaticity coordinates of (0.12, 0.50) and (0.10, 0.27) under the same excitation conditions, showing a comparable trend. The shift in chromaticity with varying excitation wavelengths suggests that both Py–Thio–Tri and Py–Thio–PyD CMPs exhibit excitation-dependent emission behavior, indicative of the presence of multiple emissive states or energy relaxation pathways.

The slight differences in emission intensity and spectral breadth between Py–Thio–Tri CMP and Py–Thio–PyD CMP can be linked to their structural variations. The biphenyl units in Py–Thio–Tri CMP provide a larger π-conjugated system compared to the pyridine units in Py–-Thio–Tri CMP, which might affect the degree of intramolecular charge transfer (ICT) and the stabilization of excited states. The nitrogen atoms in the pyridine units of Py–Thio–PyD CMP, being more electron-withdrawing, could enhance donor-acceptor interactions, potentially leading to subtle differences in the energy levels and the efficiency of non-radiative decay pathways. Hence, it can be concluded that while Py–Thio–Tri CMP and Py–Thio–PyD CMP share similar emission maxima, their spectral profiles and chromaticity coordinates are influenced by both their structural differences and the excitation wavelength. This behavior underscores the role of structural design in tuning the optical properties of these conjugated polymers, making them promising candidates for optoelectronic applications such as light-emitting diodes and sensors, where control over emission color and intensity is critical. The UV-visible absorption and photoluminescence spectra of Py–Thio–Tri CMP and Py–Thio–PyD CMP provide complementary insights into the electronic and optical properties of these polymers. The UV-visible

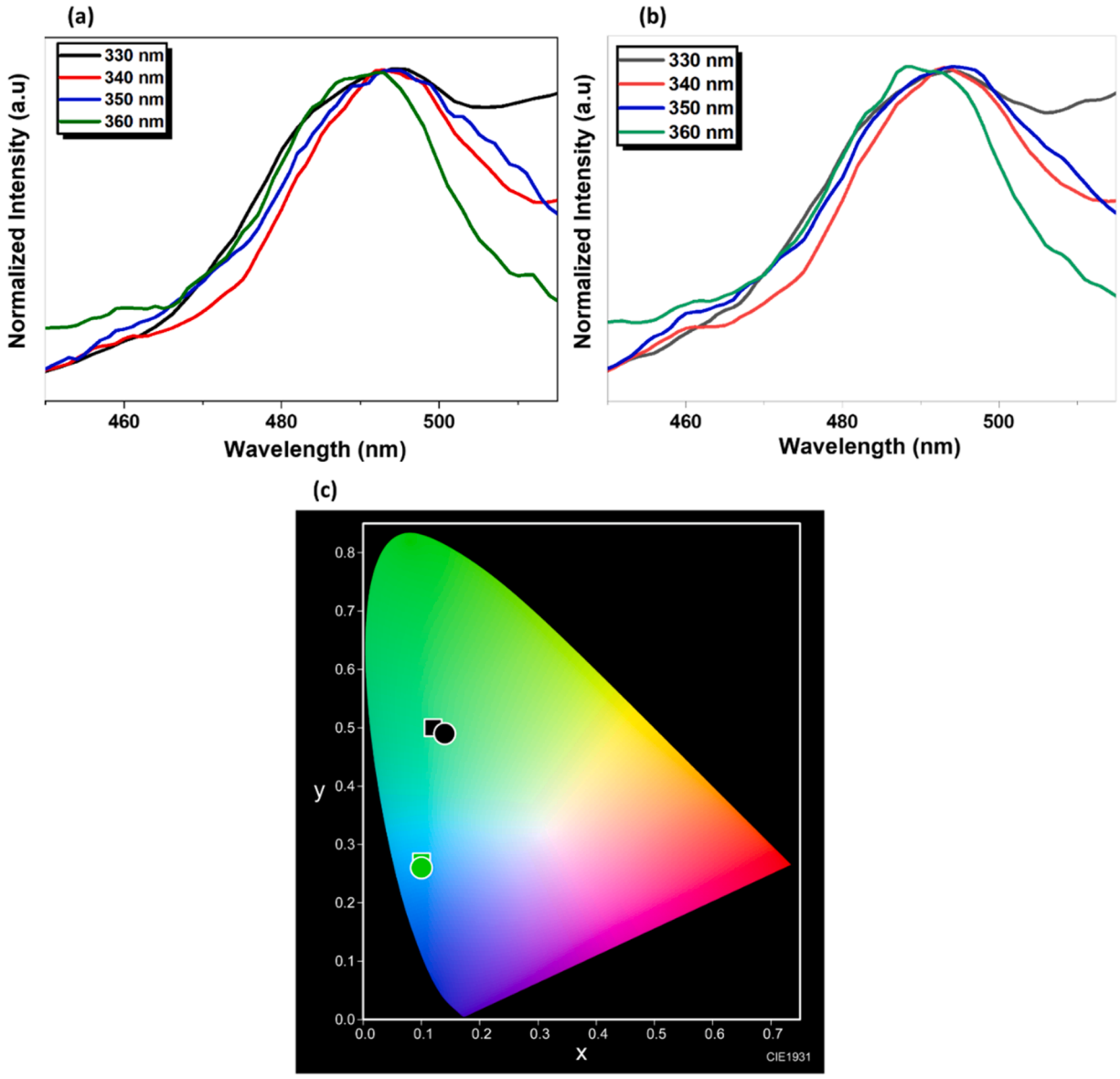

Fig. 6. Photoluminescence spectra of the Py–Thio–Tri CMP (a) and Py–Thio–PyD CMP (b) in the solid state at different excitation wavelengths. (c) CIE chromaticity diagram of the emission colors at selected excitation wavelengths.

spectra revealed a strong absorption band at 305 nm for both polymers, attributed to π-π* transitions within their conjugated backbones. Additionally, shoulders observed at 385 nm and 510 nm suggest the presence of intramolecular charge transfer (ICT) transitions, which are facilitated by the donor-acceptor interactions between the electron-rich (e.g., pyrene and thiophene) and electron-deficient (e.g., triazine or pyridine) units in their structures. The excitation wavelengths used for photoluminescence measurements (330-360 nm) overlap with these absorption features, confirming that the emission originates from the excited electronic transitions within this range. The emission spectra of both polymers exhibit maxima between 490 and 495 nm, corresponding to radiative decay from the lowest excited state (S1). The significant Stokes shift observed between the absorption maximum (305 nm) and the emission maximum (495 nm) reflects energy losses due to vibrational relaxation and non-radiative decay pathways before photon emission. This large Stokes shift indicates substantial structural reorganization in the excited state, which is characteristic of systems with strong donor-acceptor interactions. The similarity in emission maxima for Py–-Thio–Tri CMP and Py–Thio–PyD CMP suggests that their primary emissive states are not significantly affected by the substitution of biphenyl units in Py–Thio–Tri CMP with pyridine units in Py–Thio–PyD CMP. The structural differences between the two polymers, however, do influence their optical properties in subtle ways. Py–Thio–PyD CMP exhibits higher absorbance at 305 nm compared to Py–Thio–Tri CMP, which is attributed to the stronger electron-withdrawing nature of the pyridine units. Furthermore, the excitation-dependent emission behavior provides additional insights into their relaxation dynamics. When excited at 330 nm (closer to the high-energy π-π* transition at 305 nm), both polymers exhibit broader emission spectra with stronger intensities at wavelengths longer than 490 nm. This behavior suggests the involvement of higher-energy electronic states or enhanced vibrational relaxation pathways. In contrast, excitation at 360 nm (closer to the ICT transition shoulder at 385 nm) results in narrower emission spectra with diminished intensity at longer wavelengths, indicating a selective population of lower-energy electronic states. These results highlight the correlation between the UV-visible absorption and photoluminescence spectra, highlighting the interplay between the electronic structures of Py–Thio–Tri CMP and Py–Thio–PyD CMP and their ability to absorb and emit light. The similarities in their absorption spectra suggest a similar electronic environment, while the differences in their emission

behavior, particularly at varying excitation wavelengths, provide insights into their distinct photophysical properties. Collectively, the UV-visible and photoluminescence spectra demonstrate the potential of Py–Thio–Tri CMP and Py–Thio–PyD CMP as promising candidates for optoelectronic applications, particularly in devices requiring tunable light emission in the visible range. **Figure S8** presents the photoluminescence (PL) spectra of Py–Thio–Tri CMP and Py–Thio–PyD CMP incorporating 3 wt % Co. Both samples exhibit a prominent emission peak centered around 440 nm. Additionally, the Py–Thio–PyD CMP with 3 wt % Co shows a broader secondary emission peak at approximately 556 nm.

2.9. Photocatalytic H_2 evolution of Py–Thio–Tri CMP and Py–Thio–PyD CMP

Based on the differences discussed in electronic structure, charge transfer capabilities, surface area, and energy levels, a logical explanation for the superior hydrogen evolution efficiency of Py–Thio–Tri CMP over and Py–Thio–PyD CMP emerges, as illustrated in [Fig. 7]. This figure demonstrates the enhanced photocatalytic performance of Py–Thio–Tri CMP in comparison to Py–Thio–PyD CMP over time. Py–Thio–Tri CMP benefits from extended π-conjugation due to the presence

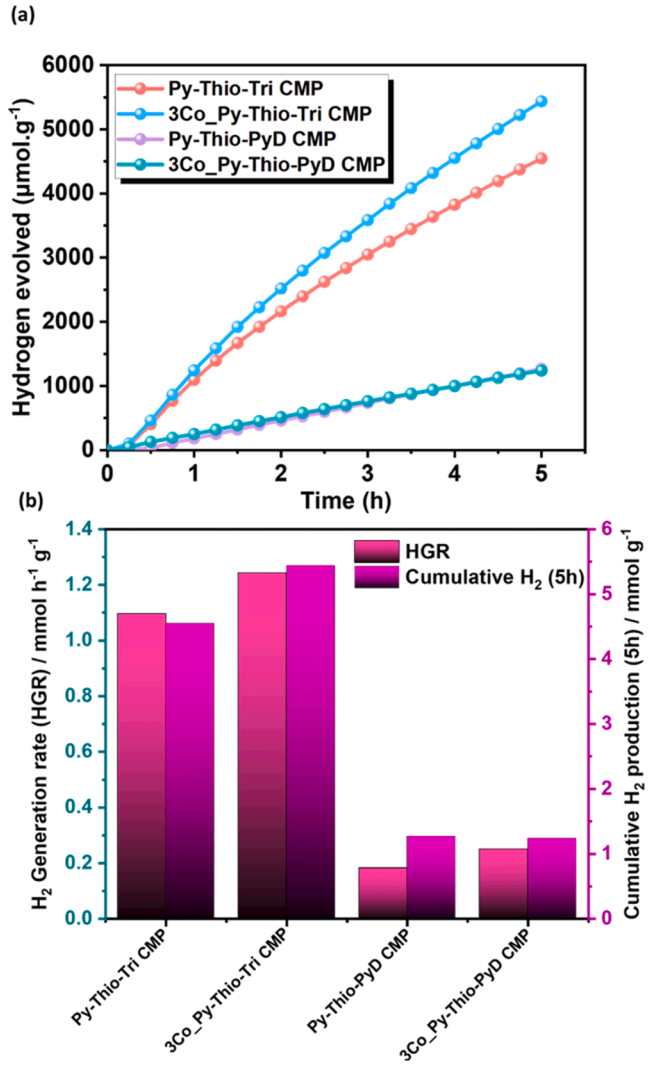

Fig. 7. (a) Time course of H_2 evolution over 5 mg Py–Thio–Tri CMP and Py–Thio–PyD CMP in a 30 % vol. aqueous methanol under UV light irradiation for 5 h. (b) Histograms of initial and cumulative hydrogen production of CMP samples.

of biphenyl units, which enhance charge delocalization, light absorption, and efficient charge transport [40]. This structural advantage leads to improved photocatalytic activity, as evidenced by the significantly higher hydrogen production observed in [Fig. 7(a)]. The initial hydrogen generation rate (HGR) within the first hour shows that Py–Thio–Tri CMP produces 1100 μmol h^{-1} g^{-1}, whereas Py–Thio–PyD CMP generates only 182 μmol h^{-1} g^{-1}. After incorporating 3 wt % cobalt (Co) cocatalysts, the HGR increased to 1242 μmol h^{-1} g^{-1} for Py–Thio–Tri CMP and 249 μmol h^{-1} g^{-1} for Py–Thio–PyD CMP, confirming the superior catalytic efficiency of Py–Thio–Tri CMP [62]. Furthermore, the charge transfer process in Py–Thio–Tri CMP is more effective due to its strong electron-donating pyrene thiophene units, which facilitate the movement of charge carriers to catalytic sites, thereby accelerating the HER [63].

In contrast, Py–Thio–PyD CMP contains pyridine groups that act as electron traps, reducing charge mobility and increasing recombination losses, ultimately limiting its photocatalytic performance. The structural arrangement of Py–Thio–Tri CMP also contributes to its higher surface area and porosity, providing more accessible active sites for H_2 evolution [62]. This results in greater interaction between the photocatalyst and reactants, further enhancing efficiency. As [Fig. 7(b)] illustrates, after 5 h, the cumulative hydrogen production for Py–Thio–Tri CMP reached 4550 μmol g^{-1}, whereas Py–Thio–PyD CMP only reached 1268 μmol g^{-1}. The addition of Co (3 wt %) cocatalyst further improved hydrogen production, with Py–Thio–Tri CMP achieving 5436 μmol g^{-1} and Py–Thio–PyD CMP reaching only 1239 μmol g^{-1}, reinforcing the significant difference in performance between the two CMP materials. The results highlight the superior efficiency of the Py–Thio–Tri CMP material in catalyzing hydrogen production under light irradiation. This impressive performance stems from its tailored molecular design, featuring pyrene-based electron donors and triazine-based electron acceptors. Such a configuration optimizes its electronic properties, including a favorable band gap, extensive absorption in the UV–visible spectrum, and efficient separation of photogenerated charge carriers. When illuminated, the Py–Thio–Tri CMP absorbs light energy, promoting electrons from the valence band (VB) to the conduction band (CB) through a π–π* electronic transition [**Figure S9**]. The presence of interfacial heterojunctions between the Py–Thio–Tri CMP framework and the Co cocatalyst [64,65] promotes rapid electron transfer from the conduction band of the Py–Thio–Tri CMP to the Co sites, where these electrons participate in the reduction of protons to molecular hydrogen. Simultaneously, the holes generated in the VB oxidize the sacrificial electron donor, ascorbic acid (AA), resulting in the generation of oxidized AA^{+} intermediates. A comparative overview of the hydrogen evolution performance of Py–Thio–Tri and Py and Thio–PyD CMPs with other reported photocatalysts is provided in Fig. 8 [49,51,66–70].

The efficiency of photocatalytic hydrogen evolution in Py–Thio–Tri CMP and Py–Thio–PyD CMP can be evaluated using transient photocurrent response and EIS Nyquist plots [Fig. 9(a) and 9(b)]. The transient photocurrent response highlights the materials' charge separation efficiency and recombination rates under light irradiation. Py–Thio–Tri CMP exhibits a significantly stronger photocurrent than Py–Thio–PyD CMP, demonstrating enhanced charge carrier generation and transport efficiency [69]. Additionally, the stability of the on/off cycles indicates that Py–Thio–Tri CMP maintains a steady photocurrent, minimizing recombination losses [71,72]. In contrast, Py–Thio–PyD CMP presents a weaker photocurrent, suggesting a less efficient charge transfer process. The superior performance of Py–Thio–Tri CMP is attributed to its extended conjugated system, an optimized HOMO–LUMO energy gap, and the presence of functional groups such as thiol (-S) and biphenyl triazine, which contribute to enhanced electron transport. The EIS Nyquist plots further confirm these observations by assessing charge transfer resistance (Rct). The smaller semicircle observed in Py–Thio–Tri CMP indicates lower charge transfer resistance and higher electron mobility, whereas Py–Thio–PyD CMP exhibits a larger semicircle, suggesting higher resistance and greater recombination losses. This is

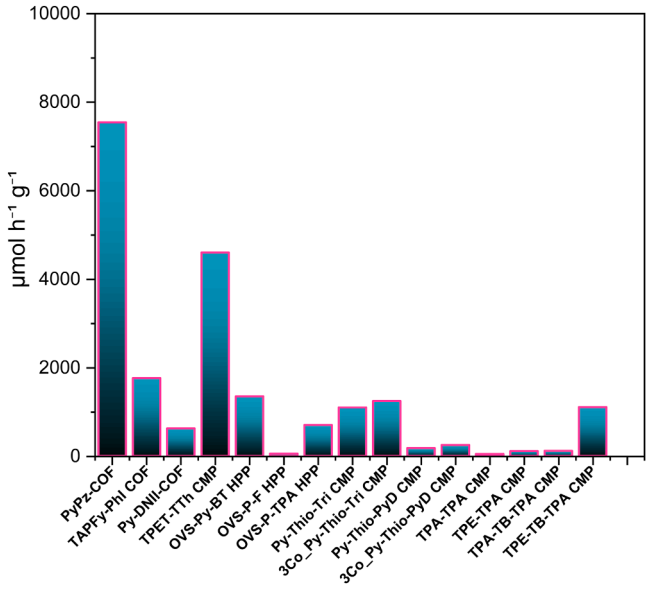

Fig. 8. A comparative summary of the hydrogen evolution activity of Py–Thio–Tri, and Thio–PyD CMPs concerning other previously reported photocatalysts.

consistent with Fig. 1, which shows that the optimized HOMO–LUMO structure in Py–Thio–Tri CMP improves charge separation and accelerates charge transfer [73]. Overall, Py–Thio–Tri CMP exhibits superior photocatalytic efficiency compared to Py–Thio–PyD CMP, owing to its higher photocurrent, lower charge transfer resistance, and favorable molecular structure. With a photocurrent of 10.8 µA cm^{-2} compared to 8.2 µA cm^{-2} for Py–Thio–PyD CMP, Py–Thio–Tri CMP is more effective at generating and separating charge carriers, leading to a greater availability of light-induced excitons for H_2 production [71,72]. The Nyquist plot results reinforce this advantage, as Py–Thio–Tri CMP's lower charge transfer resistance enables more efficient electron migration from the photocatalyst to reaction sites, thereby reducing recombination losses and improving H_2 evolution efficiency [50]. The molecular design of Py–Thio–Tri CMP further enhances its performance, with an extended conjugated system and well-aligned HOMO–LUMO energy levels promoting better visible-light absorption and charge transport.

FTIR analysis was conducted to assess the stability of Py–Thio–Tri CMP following photocatalytic testing. As shown in **Figure S10**, the spectra confirmed the preservation of all characteristic absorption bands corresponding to aromatic C–H and C=C groups. The morphologies of Py–Thio–Tri CMP and Py–Thio–PyD CMP were examined by SEM after the photocatalytic H_2 evolution experiments [**Figure S11**]. The SEM images revealed that both materials retained their structural integrity and exhibited uniform nanorod-like morphologies. These nanorods appeared to be densely packed and aligned in a relatively consistent orientation, indicating good morphological stability of the CMP frameworks under photocatalytic conditions. **Figure S12** presents the HOMO–LUMO isosurface maps of Tri-3NH_2, Py-Thio-4CHO, and Tri-PyD-3NH_2, providing critical insights into their electronic structures and orbital distributions. For Py-Thio-4CHO, both the HOMO and LUMO orbitals are delocalized across the entire molecular framework, with an associated energy gap of 2.80 eV. In contrast, Tri-3NH_2 and Tri-PyD-3NH_2 exhibit more localized frontier orbitals: the HOMO is primarily concentrated on the phenyl and pyridine moieties, while the LUMO is mainly localized on the triazine core. Fig. 10 illustrates the HOMO and LUMO orbital distributions of the corresponding Py–Thio–Tri CMP and Py–Thio–PyD CMP. In both cases, the HOMO is predominantly located on the pyrene unit, whereas the LUMO is largely delocalized over the triazine–imine–thiophene linkage. Notably, the Py-Thio-PyD CMP

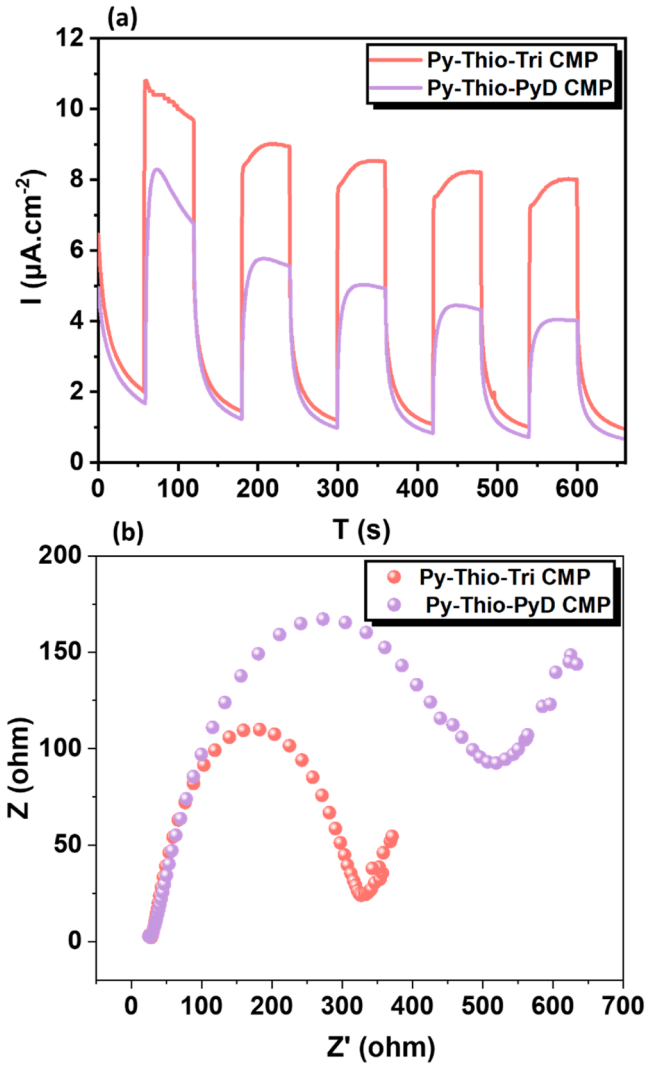

Fig. 9. (a) Transient photocurrent response (I–t) curves; (b) EIS Nyquist plots under light irradiation of Py–Thio–Tri CMP and Py–Thio–PyD CMP.

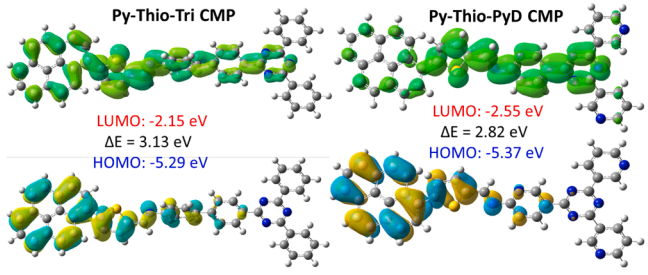

Fig. 10. The HOMO and LUMO isosurface maps of Py-Thio-Tri CMP and Py-Thio-PyD CMP, along with their energies calculated at the B3LYP-D3(BJ)/6-31G(d) level.

demonstrates a HOMO–LUMO energy gap of 2.82 eV, which is 0.31 eV narrower than that of the Py-Thio-Tri CMP.

Fig. 11 presents the molecular electrostatic potential (MESP) maps of the molecular building blocks and their corresponding polymers. This analysis provides a quantitative representation of the electrophilic and nucleophilic regions within the molecules, thereby identifying their most reactive sites. In the MESP maps, regions with high electron density are depicted in red, indicating areas of negative electrostatic potential, while regions of low electron density appear in blue, corresponding to

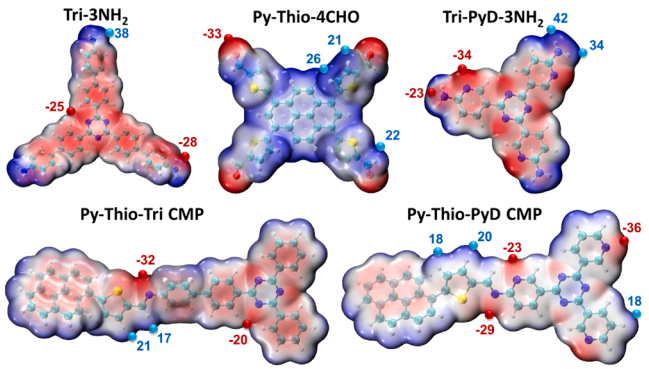

Fig. 11. MESP colored surface map with ESP surface maxima and minima (in kcal/mol) for Tri-3NH_2, Py-Thio-4CHO, Tri-PyD-3NH_2, Py-Thio-Tri CMP, and Py-Thio-PyD CMP calculated at the B3LYP-D3(BJ)/6-31G(d) level.

positive electrostatic potential. For Tri-3NH_2, the highest electron density is localized around the lone pairs of the amino nitrogen atoms, with a maximum negative potential (-28 kcal/mol). Conversely, the hydrogen atoms of the amino groups exhibit the highest positive potential (38 kcal/mol). In Tri-PyD-3NH_2, the most nucleophilic region is associated with the nitrogen atoms of the pyridine rings, which exhibit a more pronounced negative ESP of –34 kcal/mol. The hydrogen atoms of the amino groups are even more electrophilic, with a positive ESP of +42 kcal/mol, attributed to the electron-withdrawing nature of the adjacent pyridine nitrogen atoms. In Py-Thio-4CHO, the oxygen atom of the aldehyde group is the most nucleophilic site, with an ESP of –33 kcal/mol localized around its lone pairs. Upon formation of Py-Thio-Tri and Py-Thio-PyD CMPs, both the positive and negative ESP values are generally attenuated, a consequence of the extended π-conjugation and charge delocalization throughout the CMP backbone. In Py-Thio-Tri CMP, the most electrophilic region is observed around the hydrogen atoms of the thiophene rings. In contrast, the imine nitrogen atom emerges as the most nucleophilic site, with a negative ESP of –32 kcal/mol. For Py-Thio-PyD CMP, the pyridine nitrogen atoms show even higher nucleophilicity, with an ESP of –36 kcal/mol. Similar to the Py-Thio-Tri CMP, the most electrophilic sites in Py-Thio-PyD CMP are the hydrogen atoms of the thiophene units.

3. Conclusion

In summary, the successful synthesis of Py–Thio–Tri CMP and Py–-Thio–PyD (D-A) CMPs via Schiff-base condensation under solvothermal conditions has enabled a direct comparison of structural design impacts on photocatalytic H_2 evolution. Py–Thio–Tri CMP, featuring a more favorable donor–acceptor (D–A) architecture, exhibited superior photocatalytic activity with an initial H_2 generation rate (HGR) of 1100 μmol h^{-1} g^{-1}, significantly outperforming Py–Thio–PyD CMP (182 μmol h^{-1} g^{-1}). Upon loading 3 wt % cobalt as a cocatalyst, the HGR further increased to 1242 and 249 μmol h^{-1} g^{-1}, respectively. Electrochemical measurements revealed that Py–Thio–Tri CMP possesses a higher transient photocurrent and lower charge transfer resistance, indicative of more efficient exciton separation and charge transport. These results highlight the critical importance of rational molecular design—specifically, the choice and arrangement of donor and acceptor units—in enhancing the photocatalytic performance of conjugated microporous polymers. The work underscores how tailored D–A frameworks can significantly improve light harvesting, charge mobility, and ultimately, solar-to-hydrogen conversion efficiency.

CRediT authorship contribution statement

Shymaa Mostafa Ebrahium: Writing – original draft, Formal analysis, Data curation. **Yang-Chin Kao:** Data curation, Conceptualization. **Haitham M El-Bery:** Investigation, Formal analysis. **Osama Younis:** Formal analysis. **Ahmed A.K. Mohammed:** Formal analysis. **Kamal I. Aly:** Supervision. **Shiao-Wei Kuo:** Supervision, Resources. **Mohamed Gamal Mohamed:** Writing – review & editing, Writing – original draft, Supervision, Methodology, Investigation, Formal analysis, Data curation, Conceptualization.

Declaration of competing interest

The authors declare that they have no known competing financial interests or personal relationships that could have appeared to influence the work reported in this paper.

Acknowledgements

This study was supported financially by the National Science and Technology Council, Taiwan, under contracts NSTC 113-2223-E-110-001- and 113-2221-E-110-012-MY3. This work was supported by the Science, Technology & Innovation Funding Authority (STDF) in Egypt as part of the research Projects (Project ID: 46993) and the Academy of Science Research & Technology (ASRT) in Egypt, Project (RESPECT_1 ID: 10019). The authors thank the staff at National Sun Yat-sen University for their assistance with the TEM (ID: EM022600) experiments.

Supplementary materials

Supplementary material associated with this article can be found, in the online version, at doi:10.1016/j.molstruc.2025.143476.

Data availability

The data that has been used is confidential.

References

[1] L. Vidas, R. Castro, Recent developments on hydrogen production technologies: state-of-the-art review with a focus on green-electrolysis, Appl. Sci. 11 (2021) 11363, https://doi.org/10.3390/app112311363.
[2] F. Naaz, T. Ahmad, Ag-doped WO_3 nanoplates as heterogenous multifunctional catalyst for glycerol acetylation, electrocatalytic and enhanced photocatalytic hydrogen production, Langmuir 39 (2023) 9300–9314, https://doi.org/10.1021/acs.langmuir.3c00386.
[3] S.K. Jain, M. Fazil, F. Naaz, N.A. Pandit, J. Ahmed, S.M. Alshehri, Y. Mao, T. Ahmad, Silver-doped SnO_2 nanostructures for photocatalytic water splitting and catalytic nitrophenol reduction, New J. Chem. 46 (2022) 2846–2857, https://doi.org/10.1039/D1NJ05432E.
[4] M. Rahman, S. Shaheen, T. Ahmad, Photocatalytic transformation of organic pollutants and remediation strategies of carbon emissions and nitrogen fixation in inland water, Mater. Today Catal. 9 (2025) 100103, https://doi.org/10.1016/j.mtcata.2025.100103.
[5] A. Mehtab, S.A. Ali, I. Sadiq, S. Shaheen, H. Khan, M. Fazil, N.A. Pandit, F. Naaz, T. Ahmad, Hydrogen energy as sustainable energy resource for carbon-neutrality realization, ACS Sustain. Resour. Manage. 1 (2024) 604–620, https://doi.org/10.1021/acssusresmgt.4c00039.
[6] S.A. Ali, T. Ahmad, Ultrafast hole trapping in Te-$MoTe_2$-$MoSe_2$/ZnO S-scheme heterojunctions for photochemical and photo-/electrochemical hydrogen production, Small 20 (2024) 2403401, https://doi.org/10.1002/smll.202403401.
[7] H. Ishaq, I. Dincer, C. Crawford, A review on hydrogen production and utilization: challenges and opportunities, Int. J. Hydrog. Energy 47 (2022) 26238–26264, https://doi.org/10.1016/j.ijhydene.2021.11.149.
[8] N. Song, J. Jiang, S. Hong, Y. Wang, C. Li, H. Dong, State-of-the-art advancements in single atom electrocatalysts originating from MOFs for electrochemical energy conversion, Chin. J. Catal. 59 (2024) 38–81, https://doi.org/10.1016/S1872-2067(23)64622-4.
[9] J. Li, J. Jia, D. Wang, H. Dong, M. Zhu, Recent research progress of MOFs-based heterostructures for photocatalytic hydrogen evolution, Chem. Eng. J. 498 (2024) 155194, https://doi.org/10.1016/j.cej.2024.155194.
[10] H. Dong, L. Tong, P. Zhang, D. Zhu, J. Jiang, C. Li, Built-in electric field intensified by photothermoelectric effect drives charge separation over Z-scheme 3D/2D In_2Se_3/PCN heterojunction for high-efficiency photocatalytic CO_2 reduction, J. Mater. Sci. Technol. 179 (2024) 251–261, https://doi.org/10.1016/j.jmst.2023.10.012.
[11] C. Li. J. Wang, L. Tong, Y. Wang, P. Zhang, M. Zhu, H. Dong, Recent progress and challenges of photocatalytic CO_2 conversion into value-added multi-carbon

products, Coord. Chem. Rev. 502 (2024) 215623, https://doi.org/10.1016/j.ccr.2023.215623.
[12] I. Dincer, C. Acar, Review and evaluation of hydrogen production methods for better sustainability, Int. J. Hydrog. Energy 40 (2015) 11094–11111, https://doi.org/10.1016/j.ijhydene.2014.12.035.
[13] P. Zhang, H. Cheng, F. Gu, S. Hong, H. Dong, C. Li, Progress on iron-series metal-organic frameworks materials towards electrocatalytic hydrogen evolution reaction, Surf. Interfaces 42 (2023) 103368, https://doi.org/10.1016/j.surfin.2023.103368.
[14] H. Dong, C. Qu, C. Li, B. Hu, X. Li, G. Liang, J. Jiang, Recent advances of covalent organic frameworks-based photocatalysts: Principles, designs, and applications. Chin, J. Catal. 70 (2025) 142–206, https://doi.org/10.1016/S1872-2067(24)60184-1.
[15] I. Sadiq, S.A. Ali, T. Ahmad, Graphene derivative-based particulate photocatalysts for energy conversion applications: current achievements, bottlenecks, and future outlook, ACS Appl. Energy Mater. 8 (2025) 5544–5563, https://doi.org/10.1021/acsaem.5c00544.
[16] Y. Yao, X. Gao, X. Meng, Recent advances on electrocatalytic and photocatalytic seawater splitting for hydrogen evolution, Int. J. Hydrog. Energy 46 (2021) 9087–9100, https://doi.org/10.1016/j.ijhydene.2020.12.212.
[17] P. Zhang, S. Hong, N. Song, Z. Han, F. Ge, G. Dai, H. Dong, C. Li, Alloy as advanced catalysts for electrocatalysis: from materials design to applications, Chin. Chem. Lett. 35 (2024) 109073, https://doi.org/10.1016/j.cclet.2023.109073.
[18] W.T. Chung, M.A. Islam, M.G. Mekhemer, A.M. Mohamed, A.F.M. Elewa, H.H. EL-Mahdy, S.W. Chou, K.C.-W.Wu Kuo, Recent advances in metal/covalent organic frameworks based materials: their synthesis, structure design and potential applications for hydrogen production, Coord. Chem. Rev. 483 (2023) 215066, https://doi.org/10.1016/j.ccr.2023.215066.
[19] K. Chang, D.T. Tran, J. Wang, K. Dong, S. Prabhakaran, D.H. Kim, N.H. Kim, J. H. Lee, Triphasic Ni_2P–Fe_2P–CoP heterostructure interfaces for efficient overall water splitting powered by solar energy, Appl. Catal. B 338 (2023) 123016, https://doi.org/10.1016/j.apcatb.2023.123016.
[20] L. Chai, S. Liu, S. Pei, C. Wang, Electrodeposited amorphous cobalt-nickel-phosphide-derived films as catalysts for electrochemical overall water splitting, Chem. Eng. J. 420 (2021) 129686, https://doi.org/10.1016/j.cej.2021.129686.
[21] J. Su, J. Zhou, L. Wang, C. Liu, Y. Chen, Synthesis and application of transition metal phosphides as electrocatalyst for water splitting, Sci. Bull. 62 (2017) 633–644, https://doi.org/10.1016/j.scib.2016.12.011.
[22] R.R. Beswick, A.M. Oliveira, Y. Yan, Does the green hydrogen economy have a water problem? ACS Energy Lett. 6 (2021) 3167–3169, https://doi.org/10.1021/acsenergylett.1c01375.
[23] A.M. Oliveira, R.R. Beswick, Y. Yan, A green hydrogen economy for a renewable energy society, Curr. Opin. Chem. Eng. 33 (2021) 100701, https://doi.org/10.1016/j.coche.2021.100701.
[24] M.E. Webber, The water intensity of the transitional hydrogen economy, Env. Res. Lett. 2 (2007) 229–269, https://doi.org/10.1088/1748-9326/2/3/034007.
[25] A.O. Mousa, M.G. Mohamed, C.H. Chuang, S.W. Kuo, Carbonized aminal-linked porous organic polymers containing pyrene and triazine units for gas uptake and energy storage, Polymers 15 (2023) 1891, https://doi.org/10.3390/polym15081891.
[26] M.G. Mohamed, S.Y. Chang, M. Ejaz, M.M. Samy, A.O. Mousa, S.W. Kuo, Design and synthesis of bisulfone-linked two-dimensional conjugated microporous polymers for CO_2 adsorption and energy storage, Molecules 28 (2023) 3234, https://doi.org/10.3390/molecules28073234.
[27] M.M. Samy, M.G. Mohamed, S.U. Sharma, S.V. Chaganti, T.H. Mansoure, J.T. Lee, T. Chen, S.W. Kuo, Constructing conjugated microporous polymers containing triphenylamine moieties for high-performance capacitive energy storage, Polymer 264 (2023) 125541, https://doi.org/10.1016/j.polymer.2022.125541.
[28] M.M. Samy, M.G. Mohamed, S.W. Kuo, Pyrene-functionalized tetraphenylethylene polybenzoxazine for dispersing single-walled carbon nanotubes and energy storage, Compos. Sci. Technol. 199 (2020) 108360, https://doi.org/10.1016/j.compscitech.2020.108360.
[29] N. Rambhujun, M.S. Salman, T. Wang, C. Pratthana, P. Sapkota, M. Costalin, Q. Lai, K.F. Aguey-Zinsou, Renewable hydrogen for the chemical industry, MRS Energy Sustain. 7 (2020) E33, https://doi.org/10.1557/mre.2020.33.
[30] S. Sharma, S. Basu, N.P. Shetti, T.M. Aminabhavi, Waste-to-energy nexus for circular economy and environmental protection: recent trends in hydrogen energy, Sci. Total Environ. 713 (2020) 136633, https://doi.org/10.1016/j.scitotenv.2020.136633.
[31] M. Gao, C.K. Peh, L. Zhu, G. Yilmaz, G.W. Ho, Photothermal catalytic gel featuring spectral and thermal management for parallel freshwater and hydrogen production, Adv. Energy Mater. 10 (2020) 2000925, https://doi.org/10.1002/aenm.202000925.
[32] A.E. Hassan, M.H. Elsayed, M.S.A. Hussien, M.G. Mohamed, S.W. Kuo, H.H. Chou, I.S. Yahia, T.A. Mohamed, Z. Wen, V_2O_5 nanoribbons/N-deficient g-C_3N_4 heterostructure for enhanced visible-light photocatalytic performance, Int. J. Hydrog. Energy 48 (2023) 9620–9635, https://doi.org/10.1016/j.ijhydene.2022.12.009.
[33] J.H. Zhang, M.J. Wei, Z.W. Wei, M. Pan, C.Y. Su, Ultrathin graphitic carbon nitride nanosheets for photocatalytic hydrogen evolution, ACS Appl. Nano Mater. 3 (2020) 1010–1018, https://doi.org/10.1021/acsanm.9b02590.
[34] P. Niu, M. Qiao, Y. Li, L. Huang, T. Zhai, Distinctive defects engineering in graphitic carbon nitride for greatly extended visible light photocatalytic hydrogen evolution, Nano Energy 44 (2018) 73–81, https://doi.org/10.1016/j.nanoen.2017.11.059.
[35] L. Zhang, Z. Jin, S. Huang, X. Huang, B. Xu, L. Hu, H. Cui, S. Ruan, Y.J. Zeng, Bio-inspired carbon doped graphitic carbon nitride with booming photocatalytic hydrogen evolution, Appl. Catal. B 246 (2019) 61–71, https://doi.org/10.1016/j.apcatb.2019.01.040.
[36] A.O. Mousa, C.H. Chuang, S.W. Kuo, M.G. Mohamed, Strategic design and synthesis of ferrocene linked porous organic frameworks toward tunable CO_2 capture and energy storage, Int. J. Mol. Sci. 24 (2023) 12371, https://doi.org/10.3390/ijms241512371.
[37] M.G. Mohamed, M.G. Kotp, A.O. Mousa, Y.S. Li, S.W. Kuo, Construction of Fe- and N-doped microporous carbon from ferrocene-based conjugated microporous polymers for supercapacitive energy storage, ACS Appl. Energy Mater. 8 (2025) 2389–2402, https://doi.org/10.1021/acsaem.4c02968.
[38] A. Basit, M.G. Mohamed, S.U. Sharma, S.W. Kuo, Thianthrene- and Thianthrene Tetraoxide-Functionalized Conjugated Microporous Polymers for Efficient Energy Storage, ACS Appl. Polym. Mater. 6 (2024) 12247–12260, https://doi.org/10.1021/acsapm.4c02368.
[39] A. Basit, M.G. Mohamed, M. Ejaz, B.X. Su, H. Manzoor, S.W. Kuo, Boosting supercapacitor energy storage using microporous carbon derived from an octavinylsilsesquioxane and fluorenone-linked porous hybrid polymer, ACS Appl. Energy Mater. 7 (2024) 7505–7516, https://doi.org/10.1021/acsaem.4c01796.
[40] M.M. Samy, M.G. Mohamed, S.U. Sharma, S.V. Chaganti, J.T. Lee, S.W. Kuo, An Ultrastable Tetrabenzonaphthalene-Linked conjugated microporous polymer functioning as a high-performance electrode for supercapacitors, J. Taiwan Inst. Chem. Eng. 158 (2024) 104750, https://doi.org/10.1016/j.jtice.2023.104750.
[41] A.O. Mousa, Z.I. Lin, S.V. Chaganti, C.H. Chuang, C.K. Chen, S.W. Kuo, M. G. Mohamed, Bifunctional imidazolium linked tetraphenylethene based conjugated microporous polymers for dynamic antibacterial properties and supercapacitor electrodes, Polym. Chem. 15 (2024) 397–411, https://doi.org/10.1039/D3PY01303K.
[42] M.G. Mohamed, C.C. Chen, M. Ibrahim, A.O. Mousa, M.H. Elsayed, Y. Ye, S.W. Kuo, Tetraphenylanthraquinone and dihydroxybenzene-tethered conjugated microporous polymer for enhanced CO_2 uptake and supercapacitive energy storage, JACS Au 4 (2024) 3593–3605, https://doi.org/10.1021/jacsau.4c00537.
[43] M.G. Mohamed, B.X. Su, S.W. Kuo, Robust nitrogen-doped microporous carbon via crown ether-functionalized benzoxazine-linked porous organic polymers for enhanced CO_2 adsorption and supercapacitor applications, ACS Appl. Mater. Interfaces 16 (2024) 40858–40872, https://doi.org/10.1021/acsami.4c05645.
[44] M.G. Mohamed, M. Ibrahim, N.P. Chen, A. Basit, Y.C. Kao, A.O. Mousa, M. M. Samy, S.W. Kuo, Tetrabenzonaphthalene and redox-active anthraquinone-linked conjugated microporous polymers as organic electrodes for enhanced energy storage efficiency, ACS Appl. Energy Mater. 7 (2024) 5582–5593, https://doi.org/10.1021/acsaem.4c01276.
[45] M.G. Mohamed, A. Basit, M. Madhu, K. Aravinthkumar, A.I. Said, D. Manoj, W. L. Tseng, S.W. Kuo, Conjugated microporous polymer containing pyrene and Dibenzo[g,p]chrysene moieties as a luminescent powerhouse for multi-target sensing and environmental safety, Microporous Mesoporous Mater. 391 (2025) 113620, https://doi.org/10.1016/j.micromeso.2025.113620.
[46] S.V. Chaganti, S.U. Sharma, M. Ibrahim, A. Basit, P.N. Singh, S.W. Kuo, M. G. Mohamed, Redox-active a pyrene-4,5,9,10-tetraone and thienyltriazine-based conjugated microporous polymers for boosting faradaic supercapacitor energy storage, J. Power Sources 627 (2025) 235848, https://doi.org/10.1016/j.jpowsour.2024.235848.
[47] M.H. Lin, M.G. Mohamed, C.J. Lin, Y.J. Sheng, S.W. Kuo, C.L. Liu, Achieving High zT with carbon nanotube/conjugated microporous polymer thermoelectric nanohybrids by meticulous molecular geometry design, Adv. Funct. Mater. 34 (2024) 2406165, https://doi.org/10.1002/adfm.202406165.
[48] M.G. Mohamed, A.F.M. EL-Mahdy, M.G. Kotp, S.W. Kuo, Advances in porous organic polymers: syntheses, structures, and diverse applications, Mater. Adv. 3 (2022) 707–733, https://doi.org/10.1039/D1MA00771H.
[49] M.G. Mohamed, M.H. Elsayed, C.J. Li, A.E. Hassan, I.M.A. Mekhemer, A.F. Musa, M.K. Hussien, L.C. Chen, K.H. Chen, H.H. Chou, S.W. Kuo, Reticular design and alkyne bridge engineering in donor–π–acceptor type conjugated microporous polymers for boosting photocatalytic hydrogen evolution, J. Mater. Chem. 12 (2024) 7693–7710, https://doi.org/10.1039/D3TA07309B. A.
[50] M.G. Mohamed, M.H. Elsayed, A.M. Elewa, A.F.M. El-Mahdy, C.H. Yang, A.A. K. Mohammed, H.H. Chou, S.W. Kuo, Pyrene-containing conjugated organic microporous polymers for photocatalytic hydrogen evolution from water, Catal. Sci. Technol. 11 (2021) 2229–2241, https://doi.org/10.1039/D0CY02482A.
[51] S.U. Sharma, M.H. Elsayed, I.M.A. Mekhemer, T.S. Meng, H.H. Chou, S.W. Kuo, M. G. Mohamed, Rational design of pyrene and thienyltriazine-based conjugated microporous polymers for high-performance energy storage and visible-light photocatalytic hydrogen evolution from water, Giant 17 (2024) 100217, https://doi.org/10.1016/j.giant.2023.100217.
[52] M.M. Samy, I.M.A. Mekhemer, M.G. Mohamed, M.H. Elsayed, K.H. Lin, Y.K. Chen, T.L. Wu, H.H. Chou, S.W. Kuo, Conjugated microporous polymers incorporating thiazolo[5,4-d]thiazole moieties for sunlight-driven hydrogen production from water, Chem. Eng. J. 446 (2022) 137158, https://doi.org/10.1016/j.cej.2022.137158.
[53] G. Liao, Y. Gong, L. Zhang, H. Gao, G.J. Yang, B. Fang, Semiconductor polymeric graphitic carbon nitride photocatalysts: the “holy grail” for the photocatalytic hydrogen evolution reaction under visible light, Energy Environ. Sci. 12 (2019) 2080–2147, https://doi.org/10.1039/C9EE00717B.
[54] Q. Sheng, X. Zhong, Q. Shang, Y.Y. Dong, J. Zhao, Y. Du, Y. Xie, Triazine-based conjugated microporous polymers with different linkage units for visible light–driven hydrogen evolution, Front. Chem. 10 (2022) 854018, https://doi.org/10.3389/fchem.2022.854018.

[55] M.G. Mohamed, T.C. Chen, S.W. Kuo, Solid-state chemical transformations to enhance gas capture in benzoxazine-linked conjugated microporous polymers, Macromolecules 54 (2021) 5866–5877, https://doi.org/10.1021/acs.macromol.1c00736.
[56] M.G. Mohamed, T.H. Mansoure, M.M. Samy, Y. Takashi, A.A.K. Mohammed, T. Ahamad, S.M. Alshehri, J. Kim, B.M. Matsagar, K.C.W. Wu, S.W. Kuo, Ultrastable conjugated microporous polymers containing benzobisthiadiazole and pyrene building blocks for energy storage applications, Molecules 27 (2022) 2025, https://doi.org/10.3390/molecules27062025.
[57] M.G. Mohamed, W.C. Chang, S.W. Kuo, Crown ether- and benzoxazine-linked porous organic polymers displaying enhanced metal ion and CO_2 capture through solid-state chemical transformation, Macromolecules 55 (2022) 7879–7892, https://doi.org/10.1021/acs.macromol.2c01216.
[58] A. Basit, Y.C. Kao, Y.A. El-Ossaily, S.W. Kuo, M.G. Mohamed, Rational engineering and synthesis of pyrene and thiazolo[5,4-d]thiazole-functionalized conjugated microporous polymers for efficient supercapacitor energy storage, J. Mater. Chem. A 12 (2024) 30508–30521, https://doi.org/10.1039/D4TA05908E.
[59] I.M.A. Mekhemer, A.M. Elewa, M.M. Elsenety, M.M. Samy, M.G. Mohamed, A. F. Musa, T.F. Huang, T.C. Wei, S.W. Kuo, B.H. Chen, S.D. Yang, H.H. Chou, Self-condensation for enhancing the hydrophilicity of covalent organic polymers and photocatalytic hydrogen generation with unprecedented apparent quantum yield up to 500 nm, Chem. Eng. J. 497 (2024) 154280, https://doi.org/10.1016/j.cej.2024.154280.
[60] M.H. Elsayed, M. Abdellah, A.Z. Alhakemy, I M.A. Mekhemer, A.E.A. Aboubakr, B. H. Chen, A. Sabbah, K.H. Lin, W.S. Chiu, S.J. Lin, C.Y. Chu, C.H. Lu, S.D. Yang, M. G. Mohamed, S.W. Kuo, C.H. Hung, L.C. Chen, K.H. Chen, H.H. Chou, Overcoming small-bandgap charge recombination in visible and NIR-light-driven hydrogen evolution by engineering the polymer photocatalyst structure, Nat. Commun. 15 (2024) 707, https://doi.org/10.1038/s41467-024-45085-6.
[61] M.G. Mohamed, I.M.A. Mekhemer, A.F.H. Selim, A. Katsamitros, D. Tasis, A. Basit, H.H. Chou, S.W. Kuo, Molecular engineering of donor–acceptor-type conjugated microporous polymers for dual effective photocatalytic production of hydrogen and hydrogen peroxide, Mater. Horiz. 12 (2025) 5917–5928, https://doi.org/10.1039/D5MH00735F.
[62] X. Gao, C. Shu, C. Zhang, W. Ma, S.B. Ren, F. Wang, Y. Chen, J.H. Zeng, J.X. Jiang, Substituent effect of conjugated microporous polymers on the photocatalytic hydrogen evolution activity, J. Mater. Chem. A 8 (2020) 2404–2411, https://doi.org/10.1039/C9TA13212K.
[63] E. Aslan, M. Karaman, G. Yanalak, H. Bilgili, M. Can, F. Ozel, I.Hatay Patir, Synthesis of novel tetrazine-based D-π-A organic dyes for photoelectrochemical and photocatalytic hydrogen evolution, J. Photochem. Photobiol. A: Chem. 390 (2020) 112301, https://doi.org/10.1016/j.jphotochem.2019.112301.
[64] S.Y. Chang, A.M. Elewa, M.G. Mohamed, I.M.A. Mekhemer, M.M. Samy, K. Zhang, H.H. Chou, S.W. Kuo, Rational design and synthesis of bifunctional Dibenzo[g,p]chrysene-based conjugated microporous polymers for energy storage and visible light-driven photocatalytic hydrogen evolution, Mater. Today. Chem. 33 (2023) 101680, https://doi.org/10.1016/j.mtchem.2023.101680.
[65] C. Shu, Y. Zhao, C. Zhang, X. Gao, W. Ma, S.B. Ren, F. Wang, Y. Chen, J.H. Zeng, J. X. Jiang, Bisulfone-Functionalized Organic Polymer Photocatalysts for High-Performance Hydrogen Evolution, ChemSusChem. 13 (2020) 369–375, https://doi.org/10.1002/cssc.201902797.
[66] F. Wang, L. Yang, X. Wang, Y. Rong, L. Yang, C. Zhang, F. Yan, Q. Wang, Pyrazine-functionalized donor–acceptor covalent organic frameworks for enhanced photocatalytic H_2 evolution with high proton transport, Small 19 (2023) 2207421, https://doi.org/10.1002/smll.202207421.
[67] G. Zhang, M. Zhao, L. Su, H. Yu, C. Wang, D. Sun, Y. Ding, Donor–acceptor covalent–organic frameworks based on phthalimide as an electron-deficient unit for efficient visible-light catalytic hydrogen evolution, ACS Appl. Mater. Interfaces 15 (2023) 20310–20316, https://doi.org/10.1021/acsami.3c00786.
[68] I.M.A. Mekhemer, M.M. Elsenety, A.M. Elewa, K.D.G. Huynh, M.M. Samy, M. G. Mohamed, D.M. Dorrah, D.C.K. Hoang, A.F. Musa, S.W. Kuo, H.H. Chou, Push–pull–pull interactions of 2D imide–imine-based covalent organic framework to promote charge separation in photocatalytic hydrogen production, J. Mater. Chem. 12 (2024) 10790–10798, https://doi.org/10.1039/D4TA01108B. A.
[69] M.G. Mohamed, M.H. Elsayed, A.E. Hassan, A. Basit, I.M.A. Mekhemer, H.H. Chou, K.H. Chen, S.W. Kuo, Hybrid porous polymers combination of octavinylsilsesquioxane/pyrene with benzothiadiazole units for robust energy storage and efficient photocatalytic hydrogen production from water, ACS Appl. Polym. Mater. 6 (2024) 5945–5956, https://doi.org/10.1021/acsapm.4c00655.
[70] M.G. Mohamed, M.H. Elsayed, Y. Ye, M.M. Samy, A.E. Hassan, T.H. Mansoure, Z. Wen, H.H. Chou, K.H. Chen, S.W. Kuo, Construction of porous organic/inorganic hybrid polymers based on polyhedral oligomeric silsesquioxane for energy storage and hydrogen production from water, Polymers 15 (2023) 182, https://doi.org/10.3390/polym15010182.
[71] J.E. Yoo, A.A. Alshehri, S. Qin, S.M. Bawaked, M.M.M. Mostafa, N. Katabathini, D. Fehn, J. Schmidt, Establishing high photocatalytic H_2 evolution from multiwalled titanate nanotubes, ChemCatChem. 12 (2020) 2951–2956, https://doi.org/10.1002/cctc.202000281.
[72] C.X. Chen, Y.Y. Xiong, X. Zhong, P.C. Lan, Z.W. Wei, H. Pan, P.Y. Su, Y. Song, Y. F. Chen, A. Nafady, Enhancing photocatalytic hydrogen production via the construction of robust multivariate Ti-MOF/COF composites, Angew. Chem. Int. Ed. 61 (2021) e202114071, https://doi.org/10.1002/anie.202114071.
[73] Q. Zhang, D. Li, Z. Zhao, K. Zheng, Q. Wang, B. Wang, X. Long, Organic small molecular heterostructures for enhanced photocatalytic hydrogen evolution via isomer engineering, J. Mater. Chem. A 11 (2023) 5937–5944, https://doi.org/10.1039/D2TA09970E.